

Cryo-analytical STEM of frozen, aqueous dispersions of nanoparticles

Martha Ilett,^a Rik Brydson,^a Andy Brown^a and Nicole Hondow^{a*}

^a School of Chemical and Process Engineering, University of Leeds, Leeds LS2 9JT, UK

* n.hondow@leeds.ac.uk

Abstract

In situ characterisation of nanoparticle dispersion and surface coatings is required to further our understanding of the behaviour of nanoparticles in aqueous suspension. Using cryogenic transmission electron microscopy (cryo-TEM) it is possible to analyse a nanoparticle suspension in the frozen, hydrated state; however, this analysis is often limited to imaging alone. This work demonstrates the first use of analytical scanning TEM (STEM) in the examination of nanoparticles captured in a layer of vitreous ice. Imaging and analysis of frozen hydrated suspensions by both STEM energy dispersive X-ray (EDX) spectroscopy and electron energy loss spectroscopy (EELS) under cryogenic conditions demonstrates the identification and separation of CeO₂, Fe₂O₃, ZnO and Ag nanoparticles in suspension. Damage caused by the electron beam was shown to occur at far higher electron fluences in STEM (<2000 e⁻/Å²) compared to CTEM (<100 e⁻/Å²) due to diffusion limited damage by the radiolysis products generated in vitreous ice. Further application of cryo-analytical STEM was undertaken on barium titanate biomarker nanoparticles dispersed in cell culture media to show the formation of a Ca and P rich coating around the nanoparticles when suspended in the media. This previously unreported coating changes the surface chemistry of the biomarkers when exposed to cells. Thus we show that the technique has the potential to advance our understanding of the fundamental behaviour of nanoparticles in complex aqueous suspensions.

Key words

cryo, analytical, EDX, EELS, nanoparticles

1. Introduction

Transmission electron microscopy (TEM) is a leading technique for nanoparticle characterisation. High resolution imaging can be used to determine the 2-D projected size and shape of nanoparticles, with spectroscopic analysis used to confirm elemental composition. Spatial mapping of the constituent elements of samples is most often achieved through the use of scanning TEM (STEM)

coupled with energy dispersive X-ray (EDX) spectroscopy and electron energy loss spectroscopy (EELS). However, due to the vacuum requirements of TEM, there are limitations in terms of *in situ* or native state analysis, specifically of solid-liquid dispersions and the associated investigation of multiphase interactions.

In order to address the need for *in situ* characterisation of nanoparticles dispersed in liquids, recent developments have led to the emergence of liquid cells for TEM. Dynamic processes such as nanoparticle growth (1), crystallisation (2) and some biological processes (3) have been captured through the application of this technology. Initial shortcomings that meant no elemental analysis or mapping could be achieved have been overcome, with Lewis *et al.* (4) successfully demonstrating the liquid cell imaging and EDX analysis of a multi-component nanoparticle suspension. There are however some limitations: the main artefact in liquid cell analysis stems from beam-induced effects that occur in the liquid suspension; for samples suspended in aqueous solution, radiolysis of water occurs rapidly upon exposure to the electron beam, yielding products of hydrated electrons (e_{h}^-) and OH^\bullet , H^\bullet and H_2^\bullet radicals within 10 ps of energy transfer between the incident electron and water molecule. These reactive species can then undergo further reactions producing additional damage products of H_2O_2 , H_3O^+ and H_2O^\bullet (5). Within microseconds these species diffuse in the solution and react with each other and with surrounding molecules and particles in the liquid (6). In addition and in the absence of competing processes, the increased level of H_3O^+ may cause a decrease in the solution pH. Although these damage mechanisms and products can be used to drive dynamic processes (7), they are highly detrimental for the accurate characterisation of the starting solution and suspended products. Irradiation induced alteration of aqueous-based suspending media will occur even at relatively low electron fluence ($<100 e^-/\text{\AA}^2$) (8). It was established that under STEM conditions operating at an averaged flux per pixel/frame close to $140 e^-/(\text{\AA}^2 \cdot s)$, nanoparticle clusters can break apart and move out of the field of view in seconds due to alterations of the nanoparticles' surface charge induced by radiolysis products generated in the suspending solution (9).

An alternative to liquid cell TEM is preparation of frozen, hydrated suspensions transferred and imaged in the TEM at temperatures of $< -165^\circ\text{C}$ (cryogenic (cryo-) TEM). A sample is blotted onto a TEM grid and plunged rapidly into a cryogen, commonly liquid ethane, such that the suspension is captured in a layer of electron transparent vitrified ice. The process of rapidly vitrifying the liquid ensures the sample is captured in its native state *i.e.* without re-dispersion or crystallization of the suspending solution or vacuum induced drying of hydrated surfaces. Cryo-TEM is commonly associated with the determination of biomolecular structures at near-atomic resolution (10) but has recently been used to investigate liquid crystal structure (11) and the ordering of aggregates of gold nanoparticles within organic solvents (12).

There are significant benefits of cryo-TEM over liquid cell TEM: First, the lower temperature of vitreous ice relative to liquid water is likely to lead to lower rates of some if not all of the reactions involved in damage mechanisms (13, 14). Thus the rate of radiation damage of both a suspending solution and the nanoparticle sample may well be reduced. In addition, radiolysis of water is a diffusion limited process (6), and the diffusion rates in an amorphous solid held below the glass transition temperature (-137°C for water) are orders of magnitude slower than in the liquid (15). Reactive species (e.g. e_h^- , OH^\bullet , H^\bullet , H_2^\bullet , H_2O_2 , H_3O^+ and H_2O^+) produced during radiolysis in vitreous ice at -165°C will diffuse more slowly than in liquid water, reducing secondary damage to the vitreous ice (16). Furthermore, provided the suspending ice remains structurally intact, the native dispersion of the particles should remain unaltered. For example, agglomeration of nanoparticles dispersed in cell culture media has been reported by this technique (17) and flattening of nanoparticle agglomerates by the blotting process pre plunge freezing can even be accounted for (18).

Cryo-TEM also removes compositional drying artefacts as well as preventing physical movement that occurs during conventional drop cast TEM sample preparation. We have previously shown that significant differences can be observed in the elemental composition information provided by EDX spectroscopy carried out on nanoparticle dispersions in cell culture media prepared via conventional or cryo methods (19). The requirement now is to improve our ability to carry out *cryo-analytical* STEM to obtain spatially resolved elemental distributions. This area of research remains in its infancy with only limited studies having used the technique (20, 21). The main consideration when carrying out cryo-analytical STEM remains however radiolysis in the vitreous ice and the consequent damage. At its most significant the ice will melt resulting in movement of nanoparticles and prior to that possible alteration to the nanoparticle structure and composition by reactive species generated in the vitrified suspending medium.

Here we present a study in which we initially used a test sample, comprising a simple nanoparticle dispersion in water to ascertain and establish the critical fluence beyond which significant damage to vitreous ice occurs in both conventional TEM (CTEM) and STEM imaging and the role fluence rate may have on this. We show that damage caused by the electron beam occurs at lower electron fluences in CTEM compared to higher flux rate STEM, suggesting that this is due to diffusion limited damage from radiolysis products generated in the vitreous ice. In addition, we assess the fluence-limited sensitivity of both cryo-STEM EDX and EEL spectroscopy and limits to spatial resolution for crystal lattice imaging. We then show the applicability of cryo-analytical STEM to the characterisation of a solid-liquid interface, using a system of barium titanate ($BaTiO_3$) biomarker nanoparticles dispersed in cell culture media, to identify a surface coating originating from the constituents of the media.

2. Materials and Methods

2.1 Sample Preparation

A model multi-nanoparticle suspension in de-ionised water was prepared containing 50 µg/ml iron (III) oxide, primary particle size 40 nm (Fluka Chemika, Lot 40095/1 22/00), 100 µg/ml cerium dioxide, primary particle size 10 nm (Joint Research Centre, NM-211), 50 µg/ml zinc oxide, primary particle size 20-60 nm (Nanotek, ZH1121W CAS #1314-13-2) and 20 µg/ml gold-silver core-shell, primary particle size 20 nm (Sigma-Aldrich silver dispersion Lot #MKB19138V), nanoparticles.

To study the interaction of solid nanoparticles and a complex, multicomponent liquid, barium titanate (BaTiO_3) nanoparticles synthesised via a hydrothermal method at 150°C for 72 h (22) were dispersed in Roswell Park Memorial Institute (RPMI) medium supplemented with 10% Fetal bovine serum (FBS) and 1% streptomycin and penicillin. A stock suspension of 1 mg/ml of BaTiO_3 nanoparticles in deionised water was diluted in complete cell culture media to 100 µg/ml and sonicated for 5 h prior to characterisation.

Samples were prepared for cryo-TEM using an FEI Vitrobot® mark IV plunge freezer. A 3.5 µl drop of suspension was placed on either a Quantifoil TEM grid (R1.2/1.3; EM Resolutions) or a lacey carbon coated TEM grid (EM resolutions), blotted at blot force 6 and then plunged into liquid ethane. A Gatan 914 cryo-holder was used for TEM and the temperature maintained below -165°C to prevent devitrification. Ice thickness was found to be variable across the grid, with analysis conducted in areas where thickness was $< \sim 200$ nm.

2.2 Cryogenic transmission electron microscopy

Cryo-TEM was conducted using an FEI Titan³ Themis G2 operating at 300 kV fitted with an FEI Super-X 4-detector EDX system, a Gatan One-View CCD and a Gatan Quantum 965 ER imaging filter. Cryo-STEM was undertaken using probe currents between 40 and 100 pA (as measured by the dose metre on the flu cam, calibrated by a Faraday cup), a convergence semi-angle of 8.2 mrad and a 23 µs dwell time with a probe size of 1.4 Å (as measured by HAADF image resolution on silicon). Bruker Esprit v1.9 software was used for cryo-EDX collection and no post-processing was carried out on any data sets reported.

Cryo-EELS was performed using either electron loss near edge structure (ELNES) or spectral imaging (SI) conditions. For ELNES conditions high signal (Hi-Res) settings in the Gatan Microscopy Suite (v. 3.0.1) (GMS) acquisition software were used equating to a 2.5 mm spectrometer entrance aperture and no binning. A dispersion of 0.25 eV/ch was used with collection and convergence angles of 21 and 8.2 mrad respectively. In order to collect the EEL spectrum the electron beam was continually

scanned over the entire image area for the total exposure time of the EEL spectrum. For the model nanoparticle system, a high loss drift tube voltage of 660 eV and a 60 s exposure was used and magnifications of 115k times or 230k times. For SI, high speed (Hi-SNR) settings in GMS software using a 5 mm spectrometer entrance aperture and 130 x vertical binning were employed. A 0.5 eV/ch dispersion was used and the collection and convergence angles were 11.2 and 8.2 mrad respectively.

For both EELS and EDX spectroscopy no sub-pixel scanning was used.

2.3 Electron flux and fluence measures

2.3.1 CTEM

Electron fluence and flux were calculated using the following equations:

$$\text{Electron fluence } (e^-/\text{\AA}^2) = N_e/A$$

$$\text{Electron flux } (e^-/(\text{\AA}^2 \cdot s)) = \text{fluence}/t$$

Where N_e is the sum of electrons in the image, obtained after the image is taken using the camera calibration in GMS, A is the total image area in \AA^2 and t the acquisition length in s for the image.

Alternatively the acquisition routine for the Gatan One-View CCD allowed a pre-set electron fluence image to be acquired.

2.3.2 STEM

Two electron fluxes have been reported, the localised electron probe flux received at each pixel in turn referred to as F_p , and the more commonly reported average electron flux referred to as F_{av} which is the flux averaged over the whole frame.

$$F_p = I/(eA_p)$$

$$F_{av} = I/(eA_f)$$

Where I is the probe current in C/s, $e = 1.602 \times 10^{-19}$ is the electron charge in C, A_p is the area of the 1.4 \AA diameter probe and A_f is the total scan area of the frame in \AA^2 . From F_{av} the total accumulated electron fluence per scan can be calculated by multiplying by t , total scan time in s, taken as the pixel dwell time multiplied by the total number of pixels.

$$\text{Total accumulated fluence } (e^-/\text{\AA}^2) = It/(eA_f)$$

3. Results and Discussion

3.1 Model nanoparticle suspension

3.1.1 Phase contrast cryo-TEM

Cryo- conventional TEM (CTEM) imaging was performed under low-dose conditions with an objective aperture (21 mrad) inserted at a total fluence for the image of $< 100 e^-/\text{\AA}^2$ (electron flux $< 20 e^-/(\text{\AA}^2 \cdot \text{s})$) and crystal lattice spacings were measured in the fast Fourier transform (FFT) of specific regions within these images (Fig. 1). The presence of CeO_2 was established by the identification of the (111), (002) and (022) lattice planes with d -spacings of 3.1 \AA , 2.7 \AA and 1.9 \AA respectively (Fig. 1 - A). Definitive confirmation of the other constituents was not possible due to the d -spacings of some lattice planes in both ZnO and Fe_2O_3 overlapping (within experimental uncertainty). A d -spacing measurement of 2.5 \AA obtained from two regions within the TEM image could correspond to either the (101) lattice plane of ZnO or the (311) lattice plane of Fe_2O_3 (Fig. 1 - C,D).

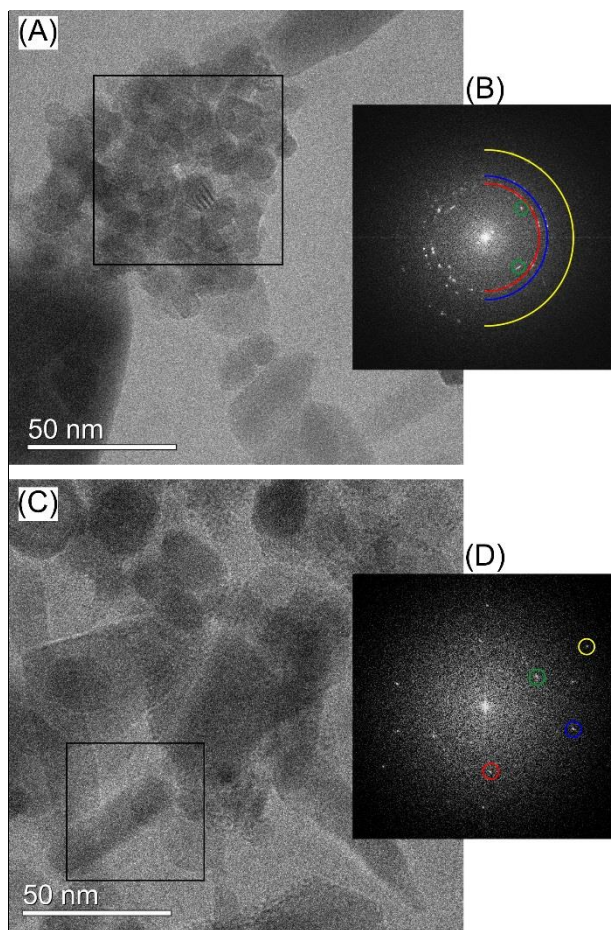


Figure 1: Cryo-CTEM images of a model nanoparticle dispersion in water containing CeO_2 , ZnO , Fe_2O_3 and Au-Ag core-shell nanoparticles. Fast Fourier transforms (FFT) were obtained from one region in each image. The area in image (A, black box) gives spots in the corresponding FFT (B) that can be attributed to CeO_2 (111) (red), (002) (blue) and (022) (yellow) and Fe_2O_3 (201) (green). The area in image (C, black box) gives spots in the corresponding FFT (D) that can be assigned to Fe_2O_3 (e.g. (201) green and (211) red), or either Fe_2O_3 or ZnO (e.g. blue Fe_2O_3 (311) or ZnO (101) and yellow (Fe_2O_3 (410) or ZnO (102)).

A magnification of 230k times was used for the images in Figure 1 and in order to prevent ice melting a very low intensity beam had to be employed (total electron fluence $<100 e^-/\text{\AA}^2$). This led to difficulties in terms of identifying and focusing the desired image. Higher magnification imaging requires a higher electron fluence to achieve similar signal to noise ratios, which for this system led to rapid destruction of the vitrified ice.

3.1.2 Cryo-STEM vs cryo-CTEM

We have observed qualitatively that under STEM conditions, a total electron fluence per frame/spectrum of similar magnitude to that used in CTEM resulted in far less damage to the ice. Exposure to a total fluence of $400 e^-/\text{\AA}^2$ in CTEM with a flux of $100 e^-/(\text{\AA}^2 \cdot \text{s})$ showed significant damage to the ice, yet after exposure to a total electron fluence of $1000 e^-/\text{\AA}^2$ in STEM with F_p of $24 \times 10^7 e^-/(\text{\AA}^2 \cdot \text{s})$ and F_{av} of $14 e^-/(\text{\AA}^2 \cdot \text{s})$, the sample showed only slight damage to the ice (Fig. 2). Beyond total fluences of $1000 e^-/\text{\AA}^2$ in STEM slight damage to the ice could be detected in the HAADF images. Total fluences, between 1500 and $4000 e^-/\text{\AA}^2$ caused more significant damage to the ice but total melting did not occur and the nanoparticles maintained the original positions in the film. In contrast, at electron fluences beyond $400 e^-/\text{\AA}^2$ in CTEM significant damage to the ice and sample movement were observed (Fig 2(B)). That higher total fluences can be used in STEM than CTEM before significant ice damage occurs is a key observation since for analytical work higher fluences will ensure better signal to noise ratios in images and EDX/EEL spectra. However, strictly this comparison should be made only on areas of the same ice thickness, with the ice damage monitored by a more quantitative measurement of either the image, diffraction pattern or spectra. Imaging would require the use of BF-STEM and reciprocity with CTEM, diffraction is challenging due to the vitreous nature of the ice but measuring changes in ice thickness upon beam exposure by low loss EELS may be a viable approach.

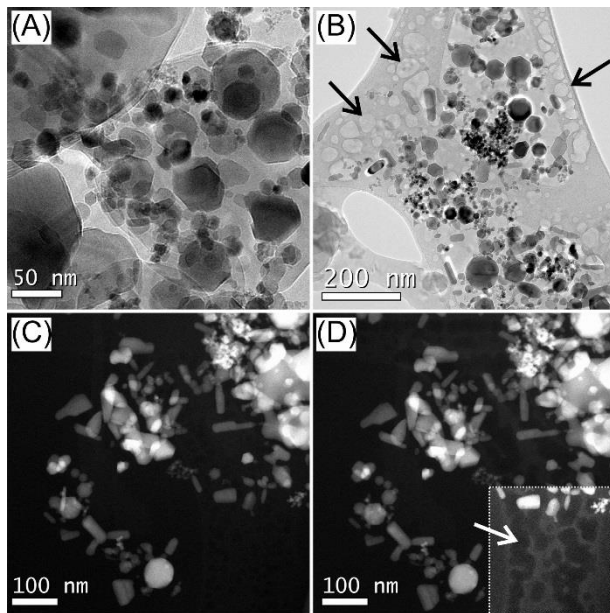


Figure 2: Qualitative assessment of the damage to the vitreous ice after exposure to definitive electron fluences in CTEM and STEM. For CTEM, images were captured using the total fluence setting. (A) At $100\text{ e}^-/\text{\AA}^2$ little to no damage was seen, (B) at $400\text{ e}^-/\text{\AA}^2$ significant damage to the ice was observed as bubbles forming in the ice indicated by the black arrows. In comparison HAADF STEM images taken before (fluence $300\text{ e}^-/\text{\AA}^2$) (C) and after (D) exposing the sample to a further fluence of $1000\text{ e}^-/\text{\AA}^2$ showed some destruction to the ice (inset in (D) after altering the contrast shows more clearly the bubbling observed in the vitreous ice indicated by the white arrow), but far less than was observed at the lower fluences in CTEM.

Clearly the focused STEM probe has significantly altered the overall damage rate in vitreous ice. STEM typically reduces charging of a sample and hence lowers the mechanical stress and specimen movement observed (23). Furthermore, although heating of the sample will be minimal, it is possible that the focused, high current density probe in STEM could cause less heating than a parallel beam, although this is thought to be dependent upon the specific probe diameter and current; it has been shown that beyond a certain dose rate, thermal heating can increase diffusion and hence result in greater damage (24). In addition, the significant differences in electron flux between STEM and CTEM could also lead to changes in damage at a given irradiation fluence of the vitreous ice. A schematic is provided (Fig. 3(A)) which postulates how damage rate might correlate to electron dose rate (or electron flux) (25). Given that radiolysis induced damage in vitreous ice (or water) is diffusion limited there will be a sublinear relationship between dose rate and damage rate where the curve plateaus at higher dose rates (*i.e.* some form of a power law dependence (with exponent < 1)). Low dose CTEM is normally carried out using an electron flux of $<10\text{ e}^-/(\text{\AA}^2\cdot\text{s})$. In comparison STEM operates with a very high localised probe flux on the order of $10^8\text{ e}^-/(\text{\AA}^2\cdot\text{s})$ for a 1.4 \AA probe

size and 60 pA probe current and even with beam broadening taken into account this is still $\sim 10^6 e^- / (\text{\AA}^2 \cdot \text{s})$ (see below and Fig. 3(B)). It should be noted here that for STEM we are referring to the probe flux (F_p) and not the average flux per frame (F_{av}), where the latter is often reported and can be orders of magnitude lower than the localised probe flux. Assuming the CTEM flux corresponds to the linear portion of the schematic and the localised STEM probe flux to the region at which the dose rate vs damage rate curve plateaus, then damage per unit fluence (*i.e.* the gradient of the curve) will be lower in STEM than CTEM, which agrees with what we have observed.

Further considerations for STEM involve broadening of the focused (sub-nanometre) probe as it traverses the specimen; we estimate, using a beam broadening equation reported by Egerton (26), that for 300 keV electrons in 100 nm thick vitreous ice, beam broadening is approximately 0.5 nm (as the ice is amorphous there will be no channelling) (Fig. 3(B)). In addition, there will be delocalised damage remote from the STEM probe position, the extent of which depends on the energy of the primary electronic excitation involved in radiolysis (and hence the spatial delocalisation of this excitation) and on the out diffusion and reactivity of the products (27). The threshold excitation energy for the radiolysis of water is 7.4 eV (28). Since the energy loss of the electron correlates inversely with the delocalisation distance then we can estimate the maximum electronic delocalisation using this threshold value (27). At 300 kV accelerating voltage, this maximum delocalisation distance is between 2-6 nm (Fig. 3(B)). Taking these factors into account and assuming significant limitation of diffusion and reactivity of damage products by operating below T_g in vitreous ice, we speculate that analogous to the leapfrog scanning method previously suggested in (29) for EELS SI of beam sensitive materials damage to the vitreous ice could be minimised by matching the specimen pixel size in STEM to the distance of delocalised damage around the broadened probe, thereby ensuring the ice is not oversampled. However, the ability to operate at this condition will be dependent upon the necessary pixel size required for resolution and the specific excitation energies of the sample. Identifying whether there is an ideal pixel size in relation to predicted delocalised damage is to be undertaken in our ongoing work, alongside quantifying damage to the ice in STEM and CTEM using areas of comparable ice thickness in order to begin to identify critical doses.

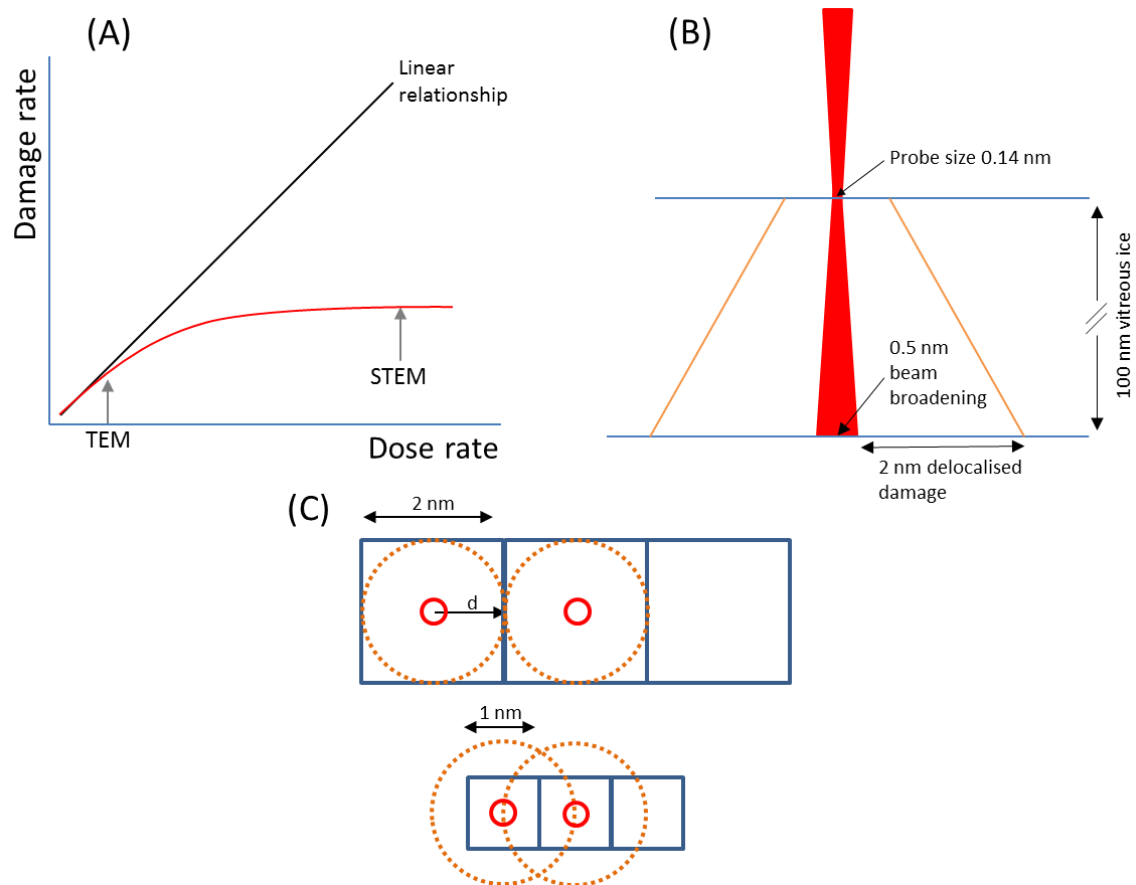


Figure 3: (A) A schematic (25) postulating the relationship between dose rate and damage rate. We speculate that the diffusion limited damage in ice corresponds to a power law relationship with exponent <1 , between damage rate and dose rate (red curve in schematic). We suggest that CTEM operates at a lower flux close to the linear portion of this curve. In comparison STEM operates at a higher flux per pixel i.e. probe flux (F_p), hence damage scales more slowly with time in STEM than CTEM and thus higher accumulated fluences are possible in STEM before significant damage to the vitreous ice is detected. (B) A schematic diagram (not to scale) showing the estimated beam broadening that will occur in STEM through 100 nm of vitreous ice, and the calculated minimum delocalised damage region (shown in orange) around the probe. (C) An alternative view of (B) showing multiple pixels with the STEM probe size and estimated delocalised damage areas (d) illustrated. Reducing the pixel size would result in the delocalised damage extending beyond the imaging pixel and oversampling would occur.

3.1.3 Cryo-STEM-EDX

Cryo-STEM-EDX analysis was used to evidence the presence of all the different types of nanoparticles in the model suspension. When operating with F_p of $40 \times 10^7 \text{ e}^-/(\text{\AA}^2 \cdot \text{s})$ and F_{av} of $3 \text{ e}^-/(\text{\AA}^2 \cdot \text{s})$ using a 3 nm pixel size and dwell time of 23 μs , a total scan time of 472 s resulted in a total electron fluence of $1300 \text{ e}^-/\text{\AA}^2$. Under these collection conditions adequate elemental signals are

obtained which allowed three out of the four nanoparticles to be identified and spatially resolved (Fig. 4 – A,B,C,D,E). Background signals corresponding to Cu and C (from the grid), as well as Si (identified as contamination from the grid boxes used both for initial grid storage and to keep the grid under liquid N₂ before transfer into the cryo holder) were detected along with clear X-ray signals corresponding to Zn, Fe and Ce. In order to obtain signals for the Au-Ag core-shell nanoparticles a higher magnification was required (Fig. 4 - G). At higher magnifications the electron fluence is increased and devitrification can become a problem. In order to combat this shorter total scan times are required. Here an additional EDX scan taken at a higher magnification (pixel size 0.93 nm) for 164 s allowed the Au-Ag core-shell nanoparticles to be mapped. This resulted in exposure to a further electron fluence of 9100 e⁻/Å² to the boxed area in Fig 4(A). However, the vitreous ice remained intact. In order to get a representative map of Au, the characteristic Au Mα X-ray peak was used since the Zn Kβ peak (9.572 keV) lies very close to the Au Lα peak (9.712 keV). This made it more difficult to obtain an adequate signal for Au and as a result the mapping did not definitively show the Au core but its presence was still confirmed through the peak detected in the spectrum.

To our knowledge an in depth discussion of fluences employed for cryo-STEM-EDX has not been carried out previously. Oleshko *et al.* (30, 31) used cryo-EDX in their studies published in 1998/9 but no discussion of electron fluence was provided, and typical scans lasted 3 h to obtain any significant signal. More recently Wolf *et al.* (21) used cryo-STEM-EDX to detect phosphorus in vitrified bacteria. They employed an electron flux F_{av} of 16×10^4 e⁻/(Å².s) but did not quote the probe flux (F_p) or total fluences for EDX acquisition. They showed significant destruction to the sample during EDX mapping but confirmation that this was due to damage to the ice or the beam sensitive nature of the organic bacteria being imaged is difficult to state without further information.

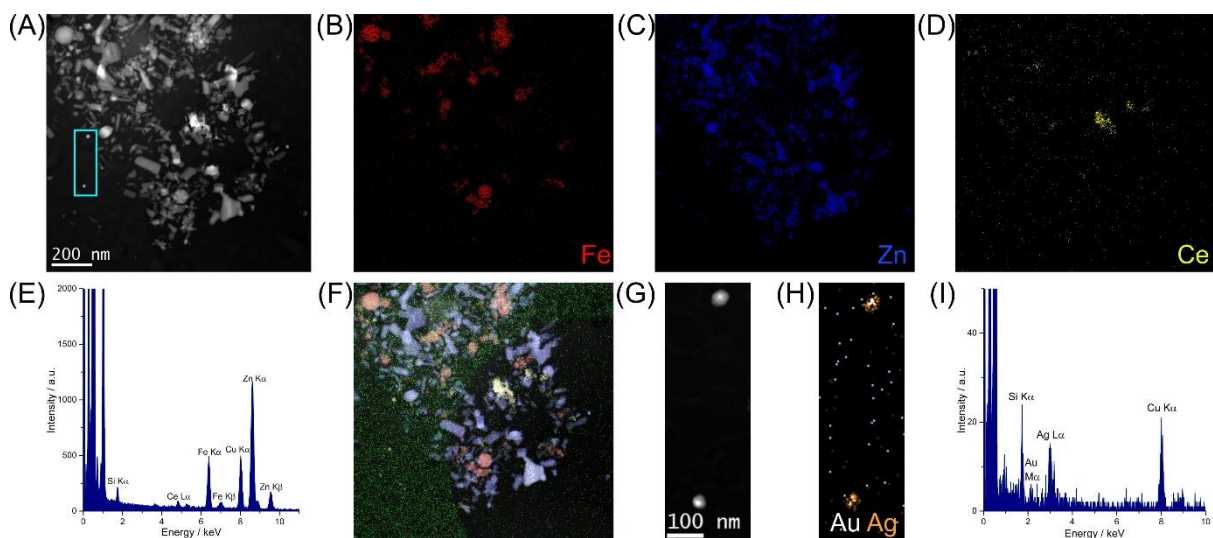


Figure 4: Cryo-EDX analysis of the model nanoparticle system collected at 100 pA for 472 s ($1300 e^-/\text{\AA}^2$) confirmed the presence of CeO_2 , Fe_2O_3 and ZnO nanoparticles. (A) HAADF STEM image of the nanoparticles analysed; (B) Fe $K\alpha$ EDX map; (C) Zn $K\alpha$ EDX map; (D) Ce $L\alpha$ EDX map and (E) EDX spectrum from the area. (F) Combined EDX maps of Fe $K\alpha$ (red), Zn $K\alpha$ (blue), Ce $L\alpha$ (yellow) and C $K\alpha$ (green). To confirm the presence of Ag-Au nanoparticles a second cryo-EDX data set was collected from the boxed region in (A); (G) HAADF STEM image; (H) Ag $L\alpha$ (orange) and Au $M\alpha$ (white) EDX maps and (I) EDX spectrum from the area. The $M\alpha$ Au signal was used rather than the $L\alpha$ to avoid the interference of the Zn $K\beta$ signal

3.1.4 Cryo-STEM-EELS

EELS can be carried out on dry samples in CTEM without significant spatial resolution (in diffraction mode), however we have already shown that even at relatively low electron fluences CTEM causes significant damage to the vitreous ice. Alternatively, EELS can be carried out using STEM and in order to preserve the vitreous ice we have had to adapt the typical SI set up parameters used for dry samples. This is because a typical SI scan using a pixel dwell time of 30 s, with a 1.3 nm pixel size and a 60 pA beam current would result in a total electron fluence on the order of $10^8 e^-/\text{\AA}^2$. We have already stated that fluences above $4000 e^-/\text{\AA}^2$ in STEM can cause damage to the vitreous ice. Therefore we have established two methods in which EELS can be carried out on vitreous samples using STEM. Firstly if little or no spatial resolution is required then for ELNES under cryo-conditions the beam can be continually scanned across the whole field of view with a dwell time of 5 μs as the spectrometer collects energy signals (averaged over the whole scanned area) for a total exposure of typically <60 s. Under these conditions total electron fluences in the order of $3000 e^-/\text{\AA}^2$ can be achieved (Fig. 5). Using this collection set-up we have successfully identified core-loss edges for Fe, Ce and Zn (Fig. 5) from the model nanoparticle system under cryo-conditions. Secondly, if high spatial resolution elemental mapping is required then alternative acquisition parameters can be used (detailed in section 2.2) which result in the loss of ELNES but retain adequate signal to map elements from the spectrum. This has been carried out in section 3.2. Cryo-EELS has been carried out previously, but this has been using only low-loss (LL) EELS (32-34). EELS is a more efficient technique than EDX due to the forward positioning of the detector. However, almost all the signal comes from the forward scattered zero-loss electrons and only a very small fraction comes from the inelastically scattered electrons which can give rise to the core-loss edges. Typical electron fluences used in previous work were in the range of 25 – $1000 e^-/\text{\AA}^2$ (34), due in part to the need to prevent damage to the beam sensitive soft matter samples being used, but also, LL EELS requires much shorter exposure times and consequently lower fluence levels than core-loss EELS to obtain

adequate electron counts. Here we have shown for the first time it is possible to carry out core-loss EELS under cryo-conditions (Fig. 5 and 7).

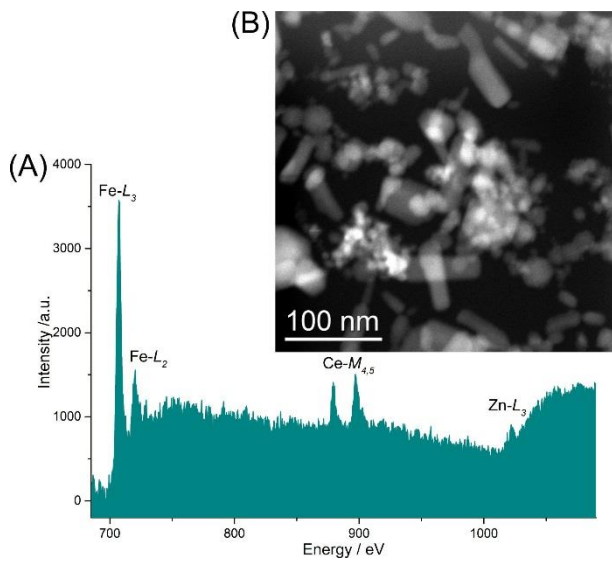


Figure 5: Cryo-EELS of the multi-nanoparticle suspension. (A) The background subtracted cryo-EEL spectrum was obtained using a 0.25 eV/ch dispersion, 2.5 mm entrance aperture, 660 eV HL drift tube with a 60 s exposure and 5 μ s dwell time at 225kx. The total electron fluence was 2000 $e^-/\text{\AA}^2$. The Fe L_{2,3} white line edge at 708 eV confirmed the presence of the Fe₂O₃ nanoparticles, the Ce M_{4,5} edge at 883-901 eV confirmed the presence of CeO₂ and the Zn L₃ edge at 1020 eV confirmed the presence of the ZnO nanoparticles. No Au or Ag edges were obtained. (B) Cryo-HAADF STEM image of the area analysed.

3.2 Application of cryo-analytical-STEM to capture solid-liquid interactions

Having established a basic protocol for STEM/EDX and EELS in vitreous ice sections, we have then applied this technique to a more relevant suspension of barium titanate (BaTiO₃) nanoparticles dispersed in cell culture media. BaTiO₃ nanoparticles have application as biomarkers in medicine, such as medical imaging and gene delivery (35). Consequently, cell uptake studies examining both the therapeutic benefit of BaTiO₃ and any potential cytotoxicity have been undertaken with nanoparticles initially dispersed in cell culture media (36, 37). This complex aqueous solution, containing a range of inorganic salts, vitamins and amino acids, is frequently supplemented with FBS which contains proteins that aid cell growth. However, significant bio-nano interactions are known to exist when nanoparticles are dispersed in cell culture media (38, 39). We have therefore been interested in applying cryo-analytical STEM to study the bio-nano interface that occurs between the BaTiO₃ nanoparticles and the complex media in an attempt to understand nanoparticle behaviour in more relevant *in vitro/in vivo* conditions.

In our previous work we have identified the formation of a calcium and phosphorus rich coating around barium titanate nanoparticles dispersed in cell culture media (19). This is thought to be an artefact of sample preparation via extended bath sonication. In addition and perhaps more importantly we found drying artefacts occurred in conventional preparation that resulted in a number of salts accumulating around the nanoparticles. Whereas a cryo sample showed that in solution, all the salts remain dissolved bar the Ca and P sources which accumulate around the nanoparticles. If not avoided by appropriate sonication this coating would change the surface chemistry of the nanoparticles when exposed to cells, potentially impacting on uptake and toxicity.

STEM-EDX mapping using a total electron fluence of $1800 e^-/\text{\AA}^2$, probe current 60 pA and 2 nm pixel size shows the previously observed coating that forms around the BaTiO₃ nanoparticles (Fig. 6). Both Na and Cl are constituents of the cell culture media and so were expected in the EDX spectrum, the mapping indicates Na was fully dispersed within the suspension. Mg is also found in cell culture and was similarly observed in the EDX spectra, however the Mg EDX map suggested it may be present in the coating seen around the BaTiO₃ nanoparticles. Mg²⁺ is known to substitute for Ca²⁺ in calcium phosphate compounds and we believe that this could be occurring here.

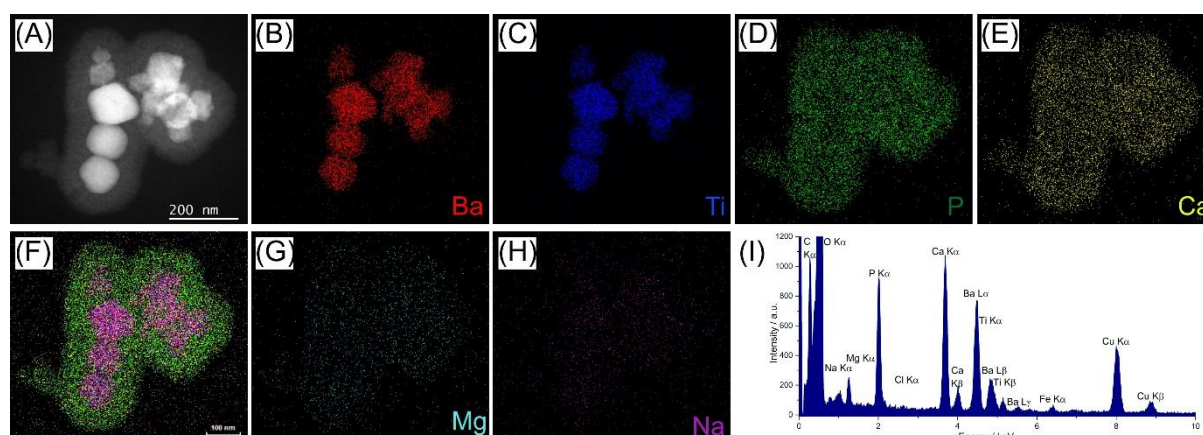


Figure 6: Cryo-EDX maps for BaTiO₃ dispersed in CCCM. A probe current of 60 pA was used, dwell time 23 μ s and total scan time 251 s. Total electron fluence was 2000 $e^-/\text{\AA}^2$. (A) The HAADF STEM image indicates the presence of a coating around the nanoparticles within suspension. EDX mapping confirmed the presence of (B) Ba and (C) Ti in the nanoparticles and identified the coating as (D) P, (E) Ca and, to a lesser extent, (G) Mg rich. (H) Na is a constituent of the media. (F) Overlaid EDX Maps of Ba L α , Ti K α , P K α and Ca K α .

In order to try and obtain more information regarding the form of the calcium phosphorus precipitate, STEM-EELS was performed. Ca L_{2,3} edges were obtained, but the P L_{2,3} edges were obscured by features extending from the Ba N_{4,5} edge that onsets at 90 eV. Detection of the P L_{2,3}

edge is compounded by difficulty in fitting a background and, in accordance with previous work, a 1st order log polynomial background was used (40).

A problem with BaTiO₃ in EDX analysis is the difficulty to resolve (or deconvolve) the Ba and Ti signals at 4.465 (*L* α) and 4.508 (*K* α) keV respectively both for elemental quantification and mapping purposes. SI EELS under cryo-conditions enables separation of the Ba and Ti signals (Fig. 7). The total electron fluence for the scan shown in Figure 7 was 2000 $e^-/\text{\AA}^2$, using a 40 pA probe current and 10 nm pixel size. A clear Ca *L*_{2,3} edge was also seen which spatially mapped to the position of the coating around the nanoparticles. Attempts were made using a low loss drift tube voltage of 130 eV to obtain the P *L*_{2,3} edge without the need for extensive post processing, but this has not yet been accomplished successfully.

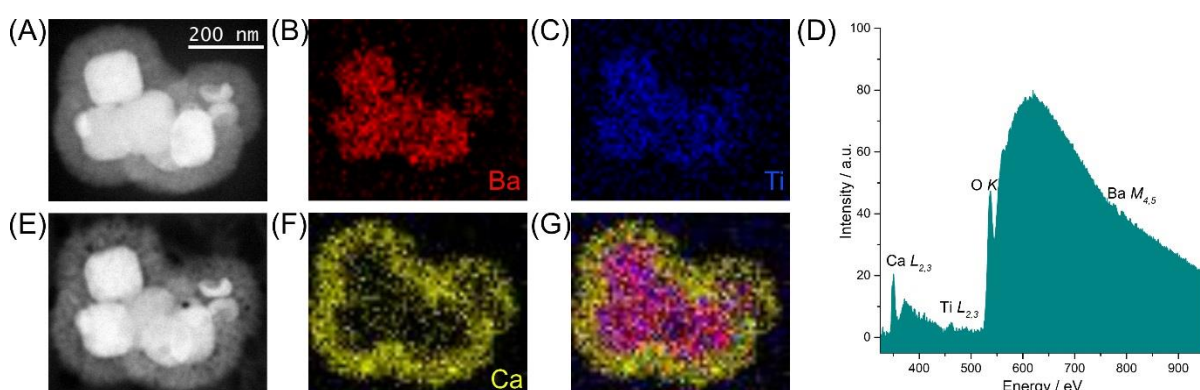


Figure 7: EELS Spectral image taken under cryo-conditions using a probe current of 40 pA, a pixel size of 10 nm and a pixel dwell time of 0.08 s, giving an overall fluence of 2000 $e^-/\text{\AA}^2$. (A) HAADF STEM image of the analysed particles; (B) Ba *M*_{4,5} map; (C) Ti *L*_{2,3} map; (D) EEL spectrum from the analysed area; (E) HAADF STEM image after analysis; (F) Ca *L*_{2,3} map; (G) combined maps of Ba *M*_{4,5} (red), Ti *L*_{2,3} (blue) and Ca *L*_{2,3} (yellow). The Ca map spatially resolves the coating around the nanoparticles. The large O *K* edge at 532 eV is due to the vitreous ice surrounding the sample. The two STEM images taken before and after the scan to monitor any significant damage to the sample showed the vitreous ice remained sufficiently intact for the particles to remain in place, but some damage effects were seen in and around the Ca-rich coating.

The electron fluences used in this work were far higher than those typically employed in biological studies. Biological cryo-TEM imaging is usually carried out using low electron fluences of $<10 e^-/\text{\AA}^2$. This however is not only to maintain the vitreous ice, it also tackles the beam sensitive nature of organic soft matter. In comparison BaTiO₃ is a dense nanomaterial which does not undergo significant beam damage and can therefore withstand the higher fluences required for spectral analysis. The fact that the high flux STEM probe outruns the diffusion induced damage generated by products of ice radiolysis more than CTEM opens up the opportunity to explore STEM and

particularly phase contrast STEM of frozen hydrated suspensions of more beam sensitive materials such as polymer coatings or even organics and pharmaceuticals (41, 42).

We have shown that the solid-liquid interactions of nanoparticles in complex biological fluids can be identified and analysed by cryo-analytical STEM of plunge frozen aqueous dispersions. The high flux rate of the STEM probe permits acquisition of good signal to noise spectra (both EDX and EELS) at fluences that induce minimal damage to the vitreous ice and insignificant movement of the encapsulated nanoparticles because of the diffusion limited damage mechanism evident in ice. This allows us to identify and understand the behaviour of nanoparticles in complex media and specifically, to monitor any changes to surface coatings. This will help facilitate continued development in the fields of both nanomedicine and nanotoxicology.

4. Conclusions

We have shown that cryo-analytical STEM is a powerful tool by which accurate native state elemental analysis of nanoparticles within a frozen, vitreous, aqueous suspension can be accomplished. It permits electron fluences up to $2000 e^-/\text{\AA}^2$ to be used without significant damage to the vitreous ice matrix. This is higher than for cryo-CTEM imaging (which is usually carried out at $< 100 e^-/\text{\AA}^2$) because of the non-linear dependence of damage rate on dose rate resulting from diffusion limited damage to vitreous ice. This is an important finding considering the fact that increased total electron fluence is key to achieving nanoscale elemental maps by STEM EDX/EEL spectroscopy. Using cryo-analytical STEM we demonstrate clear surface interaction of BaTiO_3 nanoparticles with constituents of complete cell culture media by identification of a Ca and P rich coating around the nanoparticles. This could affect the surface chemistry of biomarkers when exposed to cells and certainly demonstrates the scope and implication of the technique. Cryo-analytical STEM will provide far more relevant information than analysis of vacuum dried specimens and will continue to advance our understanding of the fundamental behaviour of nanoparticles in suspension.

Acknowledgements

The electron microscope this work was conducted on was supported by the Engineering and Physical Sciences Research Council (EPSRC), U.K. under grant EP/M028143/1. Further financial support from the EPSRC is gratefully acknowledged by NH in the form of a New Investigator Award (EP/R043388/1) and MI in the form of a studentship (Award number 1787177).

References

1. Evans, J.E. et al. Controlled growth of nanoparticles from solution with in situ liquid transmission electron microscopy. *Nano Lett.* 2011, **11**(7), pp.2809-2813.
2. Ilevlev, A.V. et al. Quantitative Description of Crystal Nucleation and Growth from in Situ Liquid Scanning Transmission Electron Microscopy. *ACS Nano.* 2015, **9**(12), pp.11784-11791.
3. de Jonge, N. et al. Electron microscopy of whole cells in liquid with nanometer resolution. *PNAS.* 2009, **106**(7), pp.2159-2164.
4. Lewis, E.A. et al. Real-time imaging and local elemental analysis of nanostructures in liquids. *Chem. Commun.* 2014, **50**(70), pp.10019-10022.
5. Schneider, N.M. et al. Electron–Water Interactions and Implications for Liquid Cell Electron Microscopy. *J. Phys. Chem. C.* 2014, **118**(38), pp.22373-22382.
6. Le Caër, S. Water Radiolysis: Influence of Oxide Surfaces on H₂ Production under Ionizing Radiation. *Water.* 2011, **3**(1), p.235.
7. Abellan, P. et al. Factors influencing quantitative liquid (scanning) transmission electron microscopy. *Chem. Commun.* 2014, **50**(38), pp.4873-4880.
8. Woehl, T.J. et al. Experimental procedures to mitigate electron beam induced artifacts during in situ fluid imaging of nanomaterials. *Ultramicroscopy.* 2013, **127**, pp.53-63.
9. White, E.R. et al. Charged Nanoparticle Dynamics in Water Induced by Scanning Transmission Electron Microscopy. *Langmuir.* 2012, **28**(8), pp.3695-3698.
10. Cheng, Y. et al. A primer to single-particle cryo-electron microscopy. *Cell.* 2015, **161**(3), pp.438-449.
11. Gao, M. et al. Direct observation of liquid crystals using cryo-TEM: Specimen preparation and low-dose imaging. *Microsc. Res. Techniq.* 2014, **77**(10), pp.754-772.
12. Balmes, O. et al. Cryo-TEM observation of 3-dimensionally ordered aggregates of 5-nm gold particles in organic solvents. *J. Nanopart. Res.* 2004, **6**(6), pp.569-576.
13. Elliot, A.J. and Bartels, D.M. *The reaction set, rate constants and g-values for the simulation of the radiolysis of light water over the range 20 deg to 350 deg C based on information available in 2008.* Canada; 2009: Atomic Energy of Canada Ltd; Report number AECL-153-127160-450-001.
14. Sterniczuk, M. and Bartels, D.M. Source of Molecular Hydrogen in High-Temperature Water Radiolysis. *The Journal of Physical Chemistry A.* 2016, **120**(2), pp.200-209.
15. Speedy, R.J. and Angell, C.A. Isothermal compressibility of supercooled water and evidence for a thermodynamic singularity at -45°C . *The Journal of Chemical Physics.* 1976, **65**(3), pp.851-858.
16. Warkentin, M. and Thorne, R.E. Glass transition in thaumatin crystals revealed through temperature-dependent radiation-sensitivity measurements. *Acta crystallographica. Section D, Biological crystallography.* 2010, **66**(Pt 10), pp.1092-1100.
17. Hondow, N. et al. Quantitative characterization of nanoparticle agglomeration within biological media. *J. Nanopart. Res.* 2012, **14**(7).
18. Wills, J.W. et al. Characterizing Nanoparticles in Biological Matrices: Tipping Points in Agglomeration State and Cellular Delivery In Vitro. *ACS Nano.* 2017, **11**(12), pp.11986-12000.

19. Ilett, M. et al. Cryo-STEM-EDX spectroscopy for the characterisation of nanoparticles in cell culture media. *J. Phys. Conf. Ser.* 2017, **902**(1), p.012006.
20. Tester, C.C. et al. In vitro synthesis and stabilization of amorphous calcium carbonate (ACC) nanoparticles within liposomes. *CrystEngComm.* 2011, **13**(12), pp.3975-3978.
21. Wolf, S.G. et al. Phosphorus detection in vitrified bacteria by cryo-STEM annular dark-field analysis. *J. Microsc.* 2015, **260**(2), pp.227-233.
22. Eckert, J.O. et al. Kinetics and mechanisms of hydrothermal synthesis of barium titanate. *J. Am. Ceram. Soc.* 1996, **79**(11), pp.2929-2939.
23. Henderson, R. and Glaeser, R.M. Quantitative analysis of image contrast in electron micrographs of beam-sensitive crystals. *Ultramicroscopy.* 1985, **16**(2), pp.139-150.
24. Egerton, R.F. and Rauf, I. Dose-rate dependence of electron-induced mass loss from organic specimens. *Ultramicroscopy.* 1999, **80**(4), pp.247-254.
25. Egerton, R.F. Radiation damage to organic and inorganic specimens in the TEM. *Micron.* 2019, **119**, pp.72-87.
26. Egerton, R.F. Limits to the spatial, energy and momentum resolution of electron energy-loss spectroscopy. *Ultramicroscopy.* 2007, **107**(8), pp.575-586.
27. Egerton, R.F. Calculation, consequences and measurement of the point spread function for low-loss inelastic scattering. *Microscopy.* 2018, **67**(suppl_1), pp.i52-i59.
28. Uehara, S. and Nikjoo, H. Monte Carlo Simulation of Water Radiolysis for Low-energy Charged Particles. *J. Radiat. Res.* 2006, **47**(1), pp.69-81.
29. Egerton, R.F. Scattering delocalization and radiation damage in STEM-EELS. *Ultramicroscopy.* 2017, **180**, pp.115-124.
30. Oleshko, V.P. et al. Combined characterization of composite tabular silver halide microcrystals by cryo-EFTEM/EELS and cryo-STEM/EDX techniques. *Microsc. Res. Techniq.* 1998, **42**(2), pp.108-122.
31. Oleshko, V.P. et al. Structural and analytical characterization of Ag(Br,I) nanocrystals by cryo-AEM techniques. *Nanostruct. Mater.* 1998, **10**(8), pp.1225-1246.
32. Kim, G. et al. Diffuse polymer interfaces in lobed nanoemulsions preserved in aqueous media. *J. Am. Chem. Soc.* 2006, **128**(20), pp.6570-6571.
33. Yakovlev, S. and Libera, M. Dose-limited spectroscopic imaging of soft materials by low-loss EELS in the scanning transmission electron microscope. *Micron.* 2008, **39**(6), pp.734-740.
34. Yakovlev, S. et al. Quantitative nanoscale water mapping in frozen-hydrated skin by low-loss electron energy-loss spectroscopy. *Ultramicroscopy.* 2010, **110**(7), pp.866-876.
35. Dempsey, C. et al. Coating barium titanate nanoparticles with polyethylenimine improves cellular uptake and allows for coupled imaging and gene delivery. *Colloids Surf., B.* 2013, **112**, pp.108-112.
36. Ciofani, G. et al. Preparation of stable dispersion of barium titanate nanoparticles: Potential applications in biomedicine. *Colloids Surf., B.* 2010, **76**(2), pp.535-543.
37. Genchi, G.G. et al. Barium titanate nanoparticles: promising multitasking vectors in nanomedicine. *Nanotechnology.* 2016, **27**(23).
38. Cedervall, T. et al. Understanding the nanoparticle–protein corona using methods to quantify exchange rates and affinities of proteins for nanoparticles. *PNAS.* 2007, **104**(7), pp.2050-2055.

39. Moore, T.L. et al. Nanoparticle colloidal stability in cell culture media and impact on cellular interactions. *Chem. Soc. Rev.* 2015, **44**(17), pp.6287-6305.
40. Wilson, A.R. Detection and quantification of low energy, low level electron energy loss edges. *Microsc. Microanal. Microstruct.* 1991, **2**(2-3), pp.269-279.
41. Sader, K. et al. Quantitative analysis of image contrast in phase contrast STEM for low dose imaging. *Ultramicroscopy.* 2010, **110**(10), pp.1324-1331.
42. Ophus, C. et al. Efficient linear phase contrast in scanning transmission electron microscopy with matched illumination and detector interferometry. *Nature communications.* 2016, **7**, pp.10719-10719.